Impact of Acceptor Quadrupole Moment on Charge Generation and Recombination in Blends of IDT-based Non-fullerene Acceptors with PCE10 as Donor Polymer

Jafar I. Khan[$1]*, Maha A. Alamoudi[$1], Neha Chaturvedi[1], Raja S. Ashraf[1,2], Mohammed N. Nabi[1], Anastasia Markina[3], Wenlan Liu[3], Top Archie Dela Peña[1,4], Weimin Zhang[1], Olivier Alévêque[5], George T. Harrison[1], Wejdan Alsufyani[1], Eric Levillain[5], Stefaan De Wolf[1], Denis Andrienko[3], Iain McCulloch[1,6], Frédéric Laquai[1]*

Dr. J. I. Khan, Dr. M. A. Alamoudi, Dr. N. Chaturvedi, Prof. R. S. Ashraf, M. N. Nabi, T. A. D. Peña, Dr. W. Zhang, Dr. G. T. Harrison, W. Alsufyani, Prof. S. D. Wolf, Prof. I. McCulloch, Prof. F. Laquai.

[1]King Abdullah University of Science and Technology (KAUST), KAUST Solar Center (KSC), Physical Sciences and Engineering Division (PSE), Thuwal 23955-6900, Kingdom of Saudi Arabia

Prof. R.S. Ashraf

[2]Department of Chemistry, Government College University Lahore, 54000, Lahore, Pakistan

Dr. A. Markina, Dr. W. Liu, Dr. D. Andrienko

[3]Max-Planck-Institut for Polymer Research (MPIP), Ackermannweg 10, D-55128 Mainz, Germany

T. A. D. Peña

[4]Department of Physics, The Hong Kong University of Science and Technology, Hong Kong, P. R. China

Dr. O. Alévêque, Prof. E. Levillian

[5]Univ Angers, CNRS, MOLTECH-ANJOU, SFR MATRIX, F-49000 Angers, France

Prof. I. McCulloch

[6]University of Oxford, Department of Chemistry, Oxford, OX1 3TA, United Kingdom

E-mail:

jafar.khan@kaust.edu.sa

frederic.laquai@kaust.edu.sa

Abstract

Advancing non-fullerene acceptor (NFA) organic photovoltaics (OPVs) requires mitigating the efficiency-limiting processes. Acceptor end-group and side-chain engineering are two handles to tune properties, yet a better understanding of their specific impact on the photophysics could facilitate a more guided acceptor design. Here, we compare the device performance, energetic landscape, and photophysics of rhodanine and dicyanovinyl end-capped IDT-based non-fullerene acceptors, namely O-IDTBR and O-IDTBCN, in PCE10-based solar cells by transient optical and electro-optical spectroscopy techniques and density functional theory calculations. We reveal how the acceptors' quadrupole moments affect the interfacial energetic landscape, in turn causing differences in exciton quenching, charge dissociation efficiencies, and geminate vs. non-geminate recombination losses. More precisely, we find that the open circuit voltage (V_{OC}) is controlled by the acceptors' electron affinity (EA), while geminate and non-geminate recombination, and the field dependence of charge generation, rely on the acceptors' quadrupole moments. We determine the kinetic parameters and yields of all processes, and demonstrate that they can reproduce the performance differences of the devices' current-voltage characteristics in carrier drift-diffusion simulations. Our results provide insight into the impact of the energetic landscape, specifically the role of the quadrupole moment of the acceptor, beyond trivial considerations of the donor-acceptor energy offsets.

Keywords: non-fullerene acceptor, ultrafast spectroscopy, quadrupole moment, organic photovoltaics, charge generation

1. Introduction

Organic photovoltaics (OPV) have recently experienced a renaissance due to the development of non-fullerene acceptors (NFAs), where single junction solar cells have now demonstrated power conversion efficiencies (PCEs) beyond 18%.[1-5] Following this recent advancement, the research focus is now on developing tailored donor and acceptor pairs that minimize the remaining quantum efficiency and energetic losses, in turn aimed to yield even higher PCEs. Yet, despite the recent increase in PCE, a precise picture of the efficiency-limiting processes in NFA-based systems is still to be revealed. Attempts towards rational design of materials are challenged by the lack of precise insight into the structure-property interplay, preventing guided (*i.e.* computer-aided / *in-silico*) material design. In this context, we recently demonstrated the impact of the acceptors' quadrupole moment on the interfacial energetics in NFA-based systems, leading to the conclusion that high internal quantum efficiencies (IQEs) require sizeable ionization energy (IE) offsets, typically in excess of 0.5 eV, since energy level bending occurs at the donor:NFA interface and reduces the exciton quenching efficiency in low IE offset systems.[6] To this end, modification of the acceptors' electron-withdrawing groups is one way of controlling the energetic landscape and acceptors' quadrupole moment, and thereby the efficiency of the exciton quenching and charge separation process. More generally, end group engineering is a common approach, that can lead to improved charge transport, as already highlighted in earlier reports.[7-11] Moreover, end-group modification such as fluorination / chlorination has led to highly-efficient systems due to enhanced electronic coupling between neighboring groups and concomitant suppression of charge recombination. [1,3,12-14]

Here, we focus on two non-fullerene acceptors, O-IDTBR, a rhodanine-endcapped indacenodithiophene (IDT),[15] and O-IDTBCN, a structural analogue, in which the rhodanine end-groups have been replaced by dicyano-vinylene moieties, in other words an indacenodithiophene donor core, flanked on either side by electron-deficient benzothiadiazole (BT) and dicyanovinyl (DCV) moieties.[8] Both NFAs were paired with PCE10 as donor polymer, a prototypical electron donor polymer allowing us to explore efficiency-limiting processes and, more importantly, their dependence on the acceptors' quadrupole moment.[16] Both donor:NFA systems ensure sizeable IE offsets, facilitating efficient exciton quenching, required to achieve high IQEs. The photovoltaic devices exhibited PCEs of 8.7% for PCE10:O-IDTBR and 9.1% for PCE10:O-IDTBCN.

Noteworthy, a drop in V_{OC} was observed upon changing from O-IDTBR to O-IDTBCN, with a net V_{OC} loss of ~0.33 V, i.e., a V_{OC} reduction from 1.07 V to 0.74 V. Contrastingly, the short circuit current density (J_{SC}) and fill factor (FF) are significantly higher in the O-IDTBCN based device. Time-resolved photoluminescence (TR-PL) measurements confirmed that, exciton quenching is efficient in O-IDTBCN-based blends (~85%), slightly less though in O-IDTBR based blends (~79%). Furthermore, nanosecond-microsecond (ns-µs) transient absorption (TA) measurements (at V_{OC} conditions) revealed the presence of nanosecond monomolecular (geminate) recombination (~33%) in the PCE10:O-IDTBR blend, which reduced to ~16% in the O-IDTBCN based blend. The origin of the higher V_{OC} in PCE10:O-IDTBR blends was investigated by determining the charge transfer (CT) state energies (E_{CT}) of both blends. The extracted values are 1.69 eV and 1.34 eV for PCE10:O-IDTBR and PCE10:O-IDTBCN devices, respectively, and thus they rationalize the difference observed in V_{OC}. Non-radiative CT state losses were found to be larger in the O-IDTBCN based device, while radiative losses were larger in the O-IDTBR based one. Time delayed collection field (TDCF) experiments confirmed that the discrepancies in the FF are caused by the difference in field dependence of charge generation. More precisely, PCE10:O-IDTBR devices exhibit field-dependent generation while PCE:O-IDTBCN devices do not. Density functional theory (DFT) calculations revealed that O-IDTBCN has a significantly larger quadrupole moment than O-IDTBR, explaining not only the differences in geminate and non-geminate recombination, but also the field dependence of CT state separation. Finally, drift-diffusion simulations demonstrated that the current density-voltage (J-V) characteristics can be reconstructed using the experimentally-obtained electro-optical parameters, indicating that spectroscopically-determined kinetic parameters and process yields can accurately describe the device physics under 1-sun illumination.[17,18]

2. Results and discussion

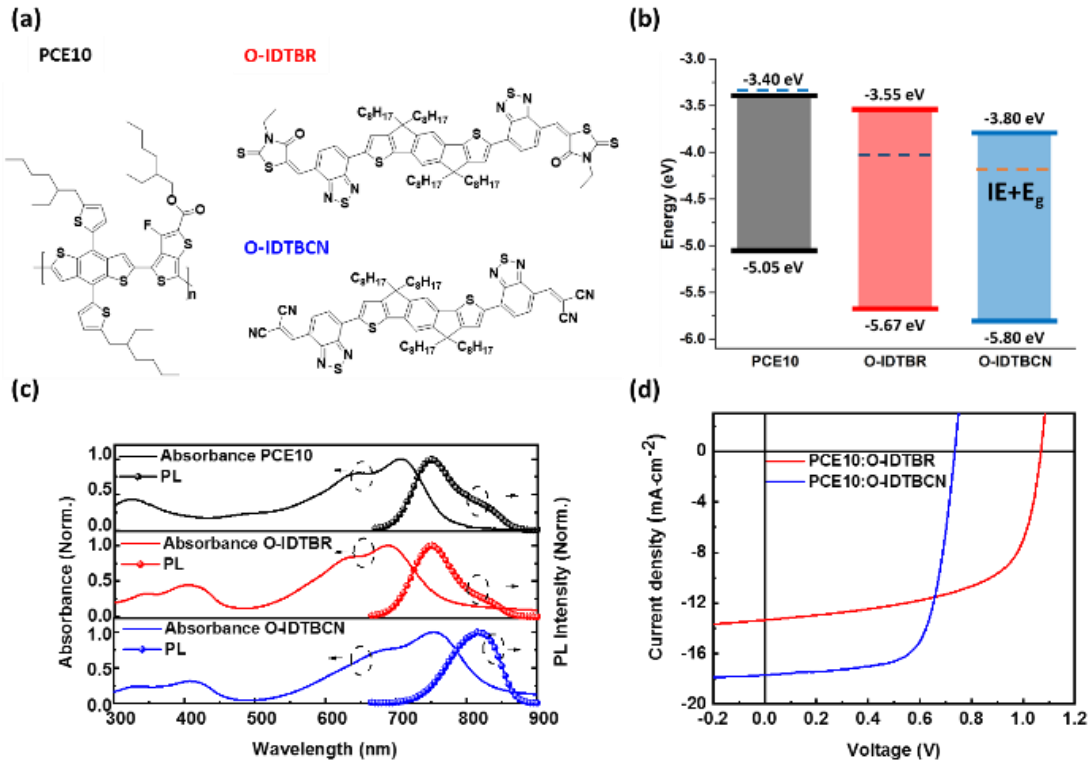

Figure 1: (a) The chemical structures of the donor polymer PCE10 and the non-fullerene acceptors O-IDTBR and O-IDTBCN, (b) the materials' IE and EA determined by UPS/LE-IPES, respectively. The dashed lines indicate the sum of IE and optical bandgap (E_g) for comparison. (c) Normalized absorption and PL spectra of neat materials, (d) measured J-V characteristics of the PCE10:O-IDTBR and PCE10:O-IDTBCN devices.

The chemical structures of the polymer (PCE10) and NFA acceptors are shown in Figure 1a. The PCE10 donor was purchased from 1-material and used as received, and the O-IDTBR non-fullerene acceptor was synthesized as reported in our previous work.[15] The O-IDTBCN acceptor differs from O-IDTBR in the replacement of rhodanine by dicyanovinyl end-groups. The synthesis protocol has been described earlier.[8] The dicyanovinyl end-group is more electron-deficient than the rhodanine, leading to an increased IE and electron affinity (EA) of O-IDTBCN compared to O-IDTBR. The IE and EA energies were measured by ultraviolet photo-electron spectroscopy / low-energy inverse photoemission spectroscopy (UPS/LE-IPES) (Figure S1) and the optical bandgap (Table 4) was estimated from the intersection of the normalized UV-vis and PL spectra

of the respective neat films, as presented in Figure 1b and 1c, to 1.71 eV for PCE10, 1.72 eV for O-IDTBR, and 1.58 eV for O-IDTBCN, respectively. The measured UV-Vis absorbance data of the blends is presented in Supporting Information Figure S2. The absorption spectrum of the pristine donor PCE10 largely overlaps with the absorption spectrum of O-IDTBR, as also shown in Figure S2. Comparing the absorption spectra of the acceptors, vibronic bands of O-IDTBR are observed peaking at 630 nm and 685 nm, respectively. Its absorption spectrum is broad, ranging from 514 to 771 nm. The absorption spectrum of O-IDTBCN is equally broad, but slightly red-shifted, covering the spectral region from 543 nm to 812 nm. Consequently, the absorption spectrum of PCE10:O-IDTBCN blends extends further into the red spectral region, peaking at 712 nm, when compared to that of PCE10:O-IDTBR blends, peaking at 685 nm. This implies that the O-IDTBCN based device can harvest more low-energy photons compared to O-IDTBR. The sizeable IE offsets of 0.62 and 0.75 eV, respectively, can facilitate a high IQE as demonstrated in our recent work on a series of related NFA-based systems.[6]

The organic solar cell (OSC) J-V characteristics (Figure 1d) show that the PCE10:O-IDTBCN based devices yield a higher J_{SC} of 17.70 $mAcm^{-2}$ and FF of 70%, but markedly lower V_{OC} of 0.74 V compared to the PCE10:O-IDTBR based devices. All figures of merit are compared in Table 1, and the external quantum efficiency (EQE) spectra of devices are shown in the Supporting Information (Figure S4); they largely resemble the blends' UV-vis absorption spectra. The variation of J_{SC} with thickness of the photoactive layer was calculated via transfer matrix analysis using *n* and *k* (refractive index, extinction coefficient) values determined by spectroscopic ellipsometry, presented in Figure S6. The maximum achievable photocurrent, $J_{SC,max}$, was determined for an active layer thickness of 90 nm (Figure S6), values are given in Table 1. The higher maximum achievable $J_{SC,max}$ of PCE10:O-IDTBCN devices is a consequence of the better complementarity to the O-IDTBCN acceptor's absorption and the further extension of its absorption into the NIR spectral range. Expectedly, the O-IDTBR based device yields higher V_{OC}, largely due to the lower EA (Figure 1b) of the acceptor O-IDTBR. However, a higher V_{OC} can also indicate less non-radiative losses in the O-IDTBR based devices (vide infra). In fact, non-radiative losses and low charge transfer state energies (E_{CT}) enhance the difference between E_{CT} and the residual energy carriers possess upon extraction (eV_{OC}), resulting in overall lower device

V_{OC}.[19] Furthermore, field dependent charge generation is observed in the O-IDTBR based blend (vide infra), accompanied by lower mobility of charge carriers.[20] This leads to the lower device J_{SC} and FF, as observed in the PCE10:O-IDTBR based devices (see Table 1).

Table 1: Figures of merit of representative inverted BHJ solar cells with a D:A blend ratio of 1:2. The device statistics were obtained by averaging over 10 solar cells. $J_{SC,max}$ corresponds to the calculated maximum achievable current density determined by transfer matrix analysis assuming 100% IQE.

Photovoltaic Blend	J_{SC} (mAcm^{-2})	V_{OC} (V)	FF (%)	$J_{SC,max}$ (mAcm^{-2})	PCE (%)
PCE10:O-IDTBR	**13.35±0.4**	**1.07±0.2**	**61±1**	**18.41**	**8.7±0.2**
PCE10:O-IDTBCN	**17.70±0.6**	**0.74±0.2**	**70±2**	**19.98**	**9.1±0.3**

Exciton dynamics from transient PL spectroscopy

Ultrafast TR-PL measurements were performed to investigate the exciton dynamics and quenching efficiency of the two blend systems. The neat polymer donor, the two acceptors, and both blends, PCE10:O-IDTBR and PCE10:O-IDTBCN, were measured following photoexcitation at 650 nm. Time-integrated PL spectra of the neat materials are presented in the SI, Figure S3. The neat O-IDTBR acceptor film exhibits a characteristic emission peak at 770 nm as reported earlier,[21] whilst the O-IDTBCN PL peaks at 814 nm. The PL of the donor PCE10 peaks at 750 nm, and the blends exhibit emission maxima at 779 nm and 810 nm (Figure 2a and 2b), respectively, which indicates residual emission from the respective acceptors and absence of donor emission.[16] For a closer analysis, the PL transients of the respective blends were tracked at the maxima of their emission peaks, shown in Figures 2c and 2d alongside the PL transients of the neat acceptors. As expected, the blends exhibit shorter PL lifetimes compared to the neat NFAs, thus confirming PL lifetime quenching, supported by the sizeable IE offsets. The PL dynamics was parametrized by the sum of two exponentials to determine the weight-averaged lifetimes. The exciton lifetimes in neat materials were found to be 313 ps for O-IDTBR and 167 ps for O-IDTBCN, they were significantly shortened to 66 ps in O-IDTBR based blends and to 25 ps in O-IDTBCN based blends. The corresponding quenching efficiency calculated by $1-(\tau_{blend}/\tau_{neat})$, where τ_{blend} and τ_{neat}

are the exciton lifetimes in blend and neat materials, respectively, was determined to 79% for PCE10:O-IDTBR and 85% for PCE10:O-IDTBCN, respectively, when the PL was tracked at the O-IDTBCN and O-IDTBR emission peaks. The efficient PL (lifetime) quenching in O-IDTBCN blends facilitates a high IQE (~80%) in devices (Figure S5). It also indicates that the main loss in the O-IDTBCN based system is due to the (still) incomplete exciton quenching. The PL quenching in the O-IDTBR based blend is slightly less and constitutes a major limitation to the IQE (~70%) of the device. Thus, a significant fraction of the J_{SC} loss is due to incomplete PL quenching, in line with the IE offset dependence of charge generation demonstrated recently by us for related NFA-based systems.[6]

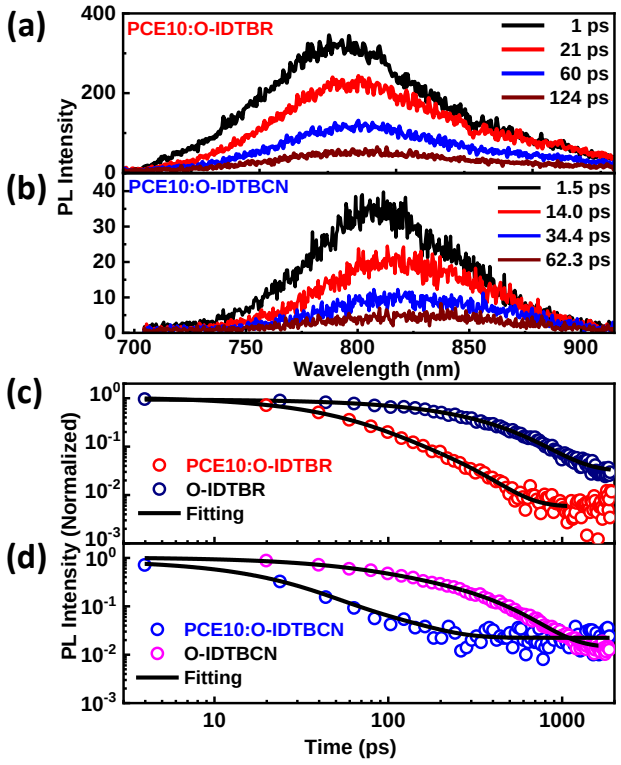

Figure 2: Time-resolved PL measurements following photoexcitation at 650 nm. (a) Time-integrated spectra of PCE10:O-IDTBR blend, (b) time-integrated spectra of PCE10:O-IDTBCN blend, (c) the associated transients tracked at the respective peak positions of the PCE10:O-IDTBR blend and the O-IDTBR neat acceptor film, (d) the transients of the PCE10:O-IDTBCN blend and the O-IDTBCN neat acceptor film.

ns-µs charge carrier recombination from transient absorption

For an in-depth comparison of the recombination losses causing the differences in J_{SC}, we carried out TA spectroscopy measurements in the nanosecond-microsecond (ns-µs) time range and subsequently evaluated the excited state dynamics. The blends were photoexcited at 532 nm, where both components of the blend absorb and the acquired TA data is presented in Figure 3. Time-integrated TA spectra of PCE10:O-IDTBR are shown in Figure 3a, here the spectral region between 1.7-2.2 eV was assigned to the ground state bleach (GSB) of the blend due to its similarity in position and shape to the steady-state absorption spectrum of the blend. The range between 0.8-1.6 eV exhibits photoinduced absorption (PA). In Figure 3b) the spectra of the PCE10:O-IDTBCN system are presented. Likewise, the spectra exhibit GSB of the blend's components between 1.7-2.2 eV. The O-IDTBCN anions appear to dominate the spectral shape in the PA range, exhibiting a sharp peak at 1.14 eV, when compared to the PCE10:O-IDTBR system, where the PA of the donor polymer PCE10 and acceptor O-IDTBR can be identified in this spectral range. The assignment of the acceptors' spectral contributions in the PA region of the TA spectra is supported by spectroelectrochemistry measurements on both acceptors (see SI Figure S7). We note that the spectral region between 1.4-1.65 eV is affected by scattered laser light used to generate the white light probe (omitted in Figure 3) in our TA experiment. Careful inspection of the PA band of the PCE10:O-IDTBR blend revealed that another component contributes to the photo-induced absorption in the range between 1-1.1 eV, evident from a spectral red shift in time, and clearly discernible after 100 ns. We assigned this contribution to triplet state formation, as discussed in more detail below. As a control experiment, TA spectra of PCE10 films doped with platinum octaethylporphyrin (PtEOP), a common triplet sensitizer, were measured, and they revealed triplet-induced absorption peaking around 1.05 eV.

We further quantified the charge carrier recombination by analysis of the associated fluence-dependent kinetics of the photovoltaic blends across the PA range; data presented in Figure 3c and 3d. The kinetics display a fluence-dependent decay across a fluence range from 0.8 to 14.8 µJ/cm^2, indicating non-geminate carrier recombination is present. A quantitative analysis was performed by global fits of the fluence-dependent dynamics of the PCE10:O-IDTBCN system to a two-pool recombination model established in our earlier works.[22] Briefly, the two-pool recombination model accounts for both geminate (fluence independent) and non-geminate (fluence dependent) recombination processes, considered as two independent populations (pools) however, spectrally

indistinguishable. As demonstrated previously, the charge density *n(t)* can be described by the following rate equation:

$$n(t) = N_0(1-f)[\exp(-k_{CT\rightarrow GS}t)] + [\lambda\gamma t + (fN_0)^{-\lambda}]^{-\frac{1}{\lambda}} \qquad (1)$$

Herein, $k_{CT\rightarrow GS}$ is the monomolecular (geminate) recombination rate constant, λ is the non-geminate recombination order, and γ is the non-geminate recombination constant, respectively, f is the fraction of separated charges that undergo non-geminate recombination, and N_0 is the total initial population of charges. The fit parameters are summarized in Table 2. However, this model cannot be readily applied to the PCE10:O-IDTBR blend as triplet dynamics is not included. The initial carrier density N_0 of the PCE10:O-IDTBCN system is calculated as described earlier by using carrier extraction data from TDCF measurements.[19] Here, the total photo-generated charge, Q_{tot}, is detected as a function of the applied laser fluence; the associated transient is presented in Figure S10. The values of the initial carrier concentration N_0 are given in Table S1. Upon globally fitting the TA dynamics, we determined that 84% of charges undergo non-geminate recombination, whereas only 16% recombine geminately in PCE10:O-IDTBCN. To compare, the maximum IQE of PCE10:O-IDTBCN is 89%, similar to the fraction of free charges observed in TA. Furthermore, from the parameters λ and γ (using a carrier concentration representative of that at one sun illumination, precisely $5\cdot10^{15}$ cm^{-3}) the strictly bimolecular ($\gamma = 2$) recombination coefficient, namely β_{TA}, was estimated to $1\cdot10^{-11}$ cm^3s^{-1} using the relation $\beta_{TA} = \gamma_\lambda n_{1sun}^{\lambda-1}$.

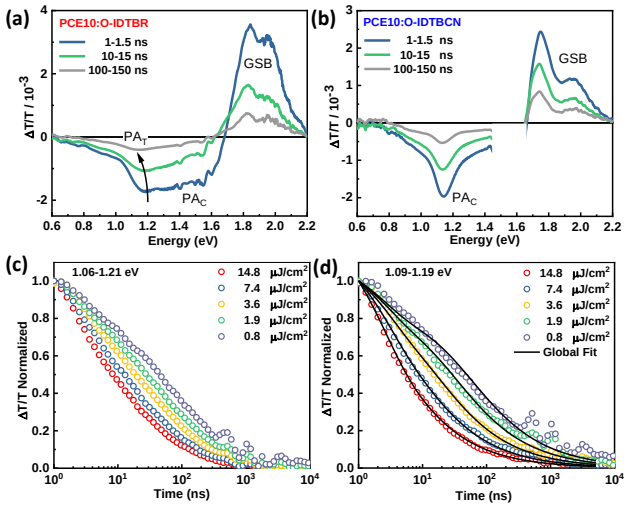

Figure 3: TA spectra and dynamics following photoexcitation at 650 nm. (a) Time-integrated TA spectra of PCE10:O-IDTBR blend, (b) time-integrated TA spectra of PCE10:O-IDTBCN blend (GSB: ground state bleach, PA_C: charge-induced absorption, PA_T: triplet-induced absorption). The region between 1.42-1.65 eV in (b) has been omitted due to scattered fundamental used for probe light generation. (c) Charge carrier dynamics for five different fluences of PCE10:O-IDTBR (open circles) probed in the spectral range of 1.06-1.21 eV, (d) charge carrier dynamics of PCE10:O-IDTBCN blend (open circles) probed in the spectral range of 1.09-1.19 eV and fitted with the two-pool model (solid black lines).

Table 2: Parameters extracted of the PCE10:O-IDTBCN blend following fitting with the two-pool model and of PCE10:O-IDTBR MCR associated charge component. Parameters are: k is the monomolecular (geminate) recombination rate constant, $\lambda+1$ is the non-geminate recombination order, γ is the non-geminate recombination coefficient, β_{TA} is the bimolecular recombination coefficient and f is the fraction of charges undergoing non-geminate recombination.

Parameter	PCE10:O-IDTBCN	PCE10:O-IDTBR
f	**0.84±0.01**	**0.67±0.01**
$1-f$	**0.16**	**0.33**
k /s^{-1}	**$4.7\cdot10^{8} \pm 3.7\cdot10^{7}$**	**$3.9\cdot10^{8} \pm 1.4\cdot10^{7}$**
$\lambda+1$	**$2.60\pm7.21\cdot10^{-4}$**	**2.15±0.0075**
γ/(cm^3)$^{\lambda}$s^{-1}	**$6.4\cdot10^{-21} \pm 8.3\cdot10^{-23}$**	**$1.1\cdot10^{-12} \pm 3.3\cdot10^{-13}$**
β_{TA} /cm^{3}s^{-1}	**$1.7\cdot10^{-11}$**	**$2.5\cdot10^{-10}$**

We further analyzed the triplet state formation in PCE10:O-IDTBR by separating the spectral features in the PA spectral range between 1.0-1.5 eV into contributions from two components. Multivariate curve resolution (MCR) analysis was used to obtained the respective component-associated spectra and dynamics of the PCE10:O-IDTBR blend.[23] To reduce the number of unknown parameters, we constrained one component to the experimentally-measured TA

spectrum of PCE10:PtEOP blends (Figure S8) and used it as input to the MCR, thus constraining the triplet-induced spectral contribution. The de-convoluted component-associated MCR spectra are displayed in Figure 4, corresponding to the charge- and triplet-induced spectral contributions. We note that in Figure 4a the triplet signal peaks at 1.05 eV, whereas the charge-induced absorption peaks at 1.17 eV. The associated normalized transients of the respective components are presented in Figure 4b. The dynamics of charges exhibit a fluence dependent decay with charges recombining within 400 ns. As the charge-induced signal decays, the triplet population rises and becomes most prominent around 2 ns. The triplet signal peaks around 4 ns for the highest fluence of 14.8 μJ/cm^2, and at 40 ns for the lowest one of 1.6 μJ/cm^2, and it decays entirely within 1 μs. The fluence dependence points to triplet state formation mostly via non-geminate charge recombination.[24,25] The formation of triplets states in PCE10:O-IDTBR and absence of triplet state formation in PCE10:O-IDTBCN can be understood when accounting for the CT state energies of both systems (vide infra). In short, the higher CT state energy of PCE10:O-IDTBR facilitates downhill triplet energy transfer from CT states to the lower energy polymer (PCE10) triplet states, unlike in PCE10:O-IDTBCN, where the lower energy CT state likely prevents polymer triplet state sensitization.

The charge carrier (component) dynamics were fitted with the same two pool model described above. The fraction of non-geminate recombination was found to be 0.67 with a non-geminate recombination coefficient β of $2.6 \cdot 10^{-10}$ cm^{3}s^{-1}. We observed that in TA the fraction of charges undergoing non-geminate recombination (~0.67) is lower than the device IQE (77%), once again indicating that there is in addition a field dependent component of charge generation. We note that TA spectroscopy is done on thin films without electrodes, effectively at V_{OC} conditions, while the IQE is determined from a device at short circuit conditions, thus in the presence of significant internal electric fields that facilitate charge separation and thereby increase the yield of the CT-to-free charge conversion process.

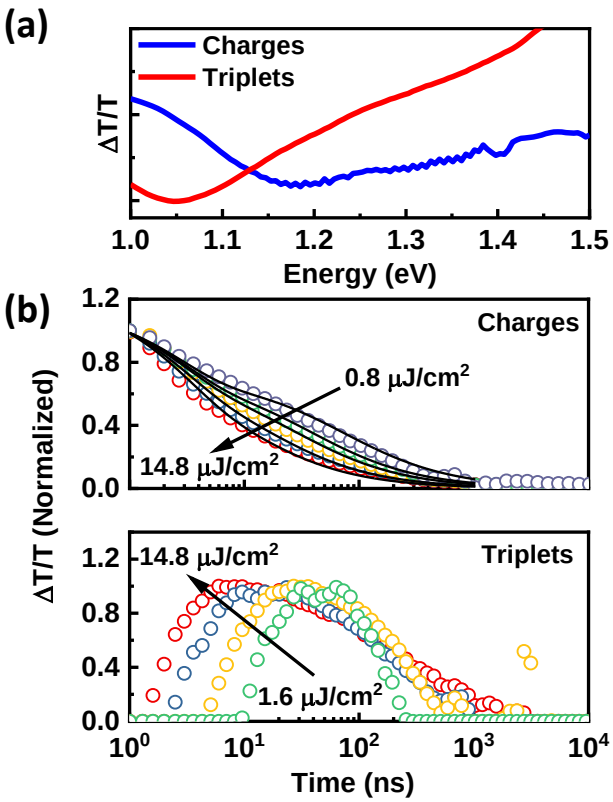

Figure 4: (a) The de-convoluted spectra from MCR analysis associated with charges (blue) and triplets (red) of the PCE10:O-IDTBR blend. (b) The normalized charge carrier dynamics of charges fitted (solid lines) using the two-pool model and triplet dynamics at different excitation fluences.

Losses reducing the open circuit voltage

Next, we address V_{OC} losses in both blends. We performed electroluminescence (EL) measurements to determine the interfacial CT state energies of the systems. The nature of the voltage losses has been discussed in recent literature.[26] Briefly, they are categorized as radiative and non-radiative losses. In this respect, the CT state energy plays a prominent role, and to a large extend it determines the device V_{OC}. Spectroscopic determination of CT state energies has previously been discussed in the pertinent literature.[27-29] Here, we applied a voltage similar to or below V_{OC} to obtain the electroluminescence spectra of the OSCs. The reduced EL spectra of the systems are presented in Figure S9. To this end, the EL intensity was converted from the

wavelength to energy scale by Jacobian conversion.[30] The EL spectrum of the O-IDTBR-based device peaks at 1.36 eV, whilst the EL of the O-IDTBCN-based device peaks at 1.02 eV.

Further evaluation of the EL spectra was done by fitting the spectra to the following function:[31]

$$\frac{I_f}{E} = \frac{f_{I_f}}{\sqrt{4\pi\lambda_{RO}kT}} \exp\left(\frac{-(E_{CT} - \lambda_{RO} - E)^2}{4\lambda_{RO}kT}\right) \quad (2)$$

where I_f (E) is the emission intensity, E is the photon energy, λ_{RO} is the reorganization energy associated with the CT process, kT is the thermal energy, f_{I_f} represents the strength of the donor/acceptor interaction, E_{CT} is the free energy difference between the CT excited state and the system's ground state. The spectrum of the O-IDTBCN system is fitted by two Gaussians accounting for the contribution from the interface (CT states) and bulk (non-fullerene acceptor) singlet state. The obtained fitting parameters are shown in Table 3. The CT state energies are determined to 1.34 eV for PCE10:O-IDTBCN and 1.69 eV for PCE10:O-IDTBR. The difference of 0.35 eV of the CT energies matches and explains the difference in V_{OC} of the O-IDTBCN based device. Furthermore, we determined the non-radiative ($q\Delta V_{OC,nonrad}$) and radiative losses ($q\Delta V_{OC,rad}$) by applying the principle of reciprocity as reported earlier.[32,33] The calculated values are given in Table 4. Sensitive EQE spectra accompanied by the EL data and the devices' external quantum efficiency (EQE_{PV}) are shown in Figure S9. More specifically, the radiative limit $V_{OC,rad}$ was calculated using equation (2) shown in the SI, yielding values of 1.18 eV and 1.26 eV for the O-IDTBCN and O-IDTBR based systems, respectively. Using equations (4) and (5) shown in the SI, $q\Delta V_{OC,nonrad}$ and $q\Delta V_{OC,rad}$ were estimated, values shown in Table 4 as well.

We conclude that the energy loss determining the V_{OC} is primarily non-radiative energy loss in O-IDTBCN based devices. The absolute value of $\Delta V_{OC,nonrad}$ is comparable to values reported in the pertinent literature.[34] Interestingly, the voltage losses in the O-IDTBR system are larger for the radiative component compared to the non-radiative component. The lower value of radiative losses in the O-IDTBCN based devices is accompanied by larger non–radiative losses leading to similar total losses in both systems. This is in good agreement with a previous works demonstrating that systems with lower CT state energy exhibit increases non-radiative losses due to fast internal conversion processes.[35]

Table 3: The parameterized values for the CT state energy (E_{CT}), the reorganization energy λ_{RO} and maximum CT emission E_{max}^{em} determined by fitting the EL spectra for the OPV devices.

Photovoltaic device	E_{CT} (eV)	λ_{RO} (eV)	E_{max}^{em} (eV)
PCE10:O-IDTBR	**1.69**	**0.26**	**1.36**
PCE10:O-IDTBCN	**1.34**	**0.08**	**1.02**

Table 4: The open circuit voltage V_{OC}, the optical bandgap E_g equivalent to the bandgap of the lowest bandgap component of the blend, the difference ΔE_{CT} between the estimated CT state energy (see table 3) and the blends' optical bandgap, and quantification of the radiative $q\Delta V_{OC,rad}$ and non-radiative $q\Delta V_{OC,nonrad}$ losses in the OPV devices.

Photovoltaic device	V_{OC} (V)	E_g (eV)	ΔE_{CT} (eV)	$q\Delta V_{OC,rad}$ (eV)	$q\Delta V_{OC,nonrad}$ (eV)
PCE10:O-IDTBR	**1.03**	**1.71**	**0.02**	**0.43**	**0.23**
PCE10:O-IDTBCN	**0.73**	**1.58**	**0.24**	**0.16**	**0.45**

Field dependence of charge generation from TDCF

Having evaluated the quantum efficiency and energy losses determining J_{SC} and V_{OC}, we now turn towards the device fill factor. To investigate the origin of differences in the device fill factor, we performed TDCF experiments on photovoltaic devices. A nanosecond laser pulse with a fluence of 0.1 µJ/cm^2 was used to generate charges in the device. After 10 ns, a collection field was applied to extract the photo-generated charges. The total extracted charge, Q_{tot}, was measured as a function of the applied bias to investigate a possible field dependence of charge generation. The acquired data is displayed in Figure 5 alongside the J-V characteristics of the particular device for variable pre-bias ranging from -1V to V_{OC}. In case of the PCE10:O-IDTBCN system, Q_{tot} remains constant as a function of the applied bias, which points to field-independent charge generation. In contrast, the collected charge decreases with pre-bias in the case of PCE10:O-IDTBR, indicating field

dependent charge generation in this system. Furthermore, when approaching the V_{OC}, non-geminate recombination losses become prevalent in both systems, as charges are no longer extracted.[36] The hole mobility ($9.8 \cdot 10^{-4}$ $cm^2V^{-1}s^{-1}$) and electron mobility ($5.2 \cdot 10^{-4}$ $cm^2V^{-1}s^{-1}$) determined by space-charge-limited current measurements are higher for the O-IDTBCN based system compared to the O-IDTBR based one, which facilitates extraction of charges. Overall, the fill factor is dictated by field dependent charge generation in the O-IDTBR based device causing significant (field-dependent) geminate recombination losses. In contrast, the O-IDTBCN based device exhibits field independent charge generation and the competition between non-geminate recombination and charge extraction is shifted towards the latter, which results in higher fill factors in devices. The lower J_{SC} in the O-IDTBR based device is in part a consequence of additional geminate losses at J_{SC} conditions.

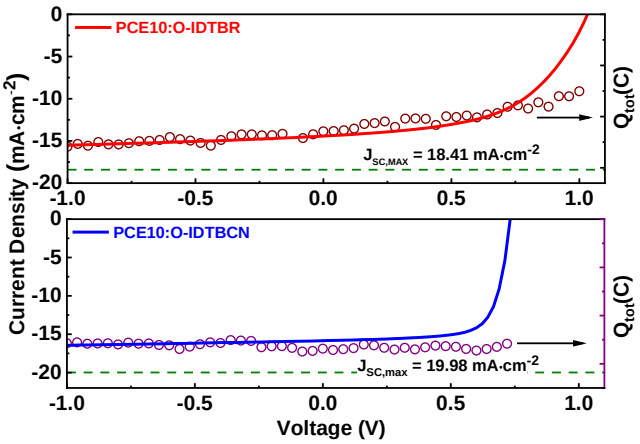

Figure 5: Time delayed collection field measurements with the total charge Q_{tot} (open circles) as a function of the applied pre-bias overlaid with the respective J-V curves (solid lines) for the representative solar cells. The dashed green lines correspond to the maximum short circuit current density for the active layer thickness of 90 nm.

We determined the bimolecular recombination coefficient, β_{TDCF}, from the TDCF measurements. Here, the collected charge, Q_{col}, was measured as a function of the time delay between photoexcitation and charge collection in the time range from 10 ns-1µs. The measured kinetics are shown in Figures S9 and S10, and the data was fitted as previously reported.[37,38] The bimolecular recombination coefficients of the respective systems were found to be $2.2 \cdot 10^{-10}$ cm^3s^{-1} for

PCE10:O-IDTBR and $1.4 \cdot 10^{-11}$ cm^3s^{-1} for PCE10:O-IDTBCN. The values are very similar to the coefficients determined by TA, i.e., $2.5 \cdot 10^{-10}$ cm^3s^{-1} and $1.7 \cdot 10^{-11}$ cm^3s^{-1}, respectively.

Finally, we demonstrate that the spectroscopically-determined kinetic parameters and yields can reproduce J-V characteristics of devices in drift-diffusion simulations. We used Setfos 4.6 (FLUXiM AG), a commercial numerical drift-diffusion device simulation tool to simulate the J-V curves as described in our previous work. [39]

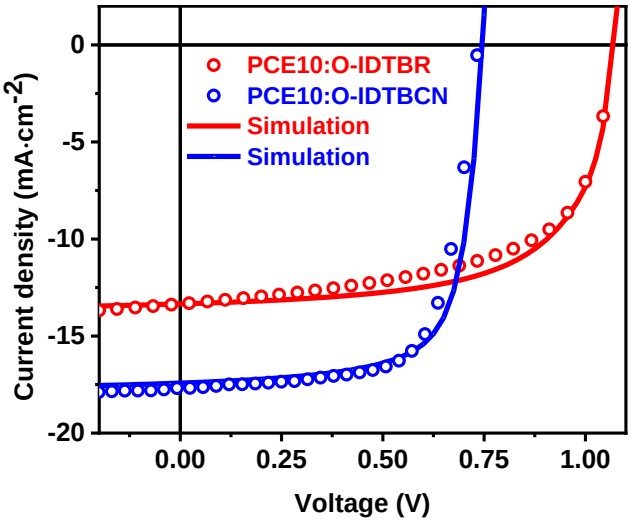

Figure 6: The J-V characteristics of representative solar cells simulated with Setfos drift-diffusion simulator software (solid lines) compared with the experimentally-obtained J-V curves (open symbols).

The input parameters of the simulation and the calculated figures-of-merit of the devices are all summarized in Table 5. The simulation was performed using the optical constants, namely the refractive index (*n*) and extinction coefficient (*k*) values (Figure S14) obtained by spectroscopic ellipsometry measurements and the hole and electron mobilities measured by space-charge-limited current (SCLC) experiments (Figure S10). The respective bimolecular recombination coefficients β_{TDCF} were obtained from TDCF (Figure S12 and S13). Furthermore, the IE and EA (Figure 1b) were determined by UPS and LE-IPES, whilst the IQE of the photovoltaic blends was determined from the EQE spectra using the relation: *IQE=EQE/(1-Reflectance-Parasitic Absorption)* and subsequently used as input parameter. The reflectance spectra of the devices were collected with an integrating sphere, the same system as used for the EQE, whereas parasitic absorption spectra were obtained from transfer matrix modelling on device structures. Using the aforementioned

parameters in the simulation, the J-V curves of the solar cells were reconstructed as they are depicted in Figure 6. The calculated figures of merit J_{SC}, V_{OC}, FF, and PCE are shown in Table 5. We note that a good agreement was obtained between the simulated J-V curves and the experimentally-measured characteristics for both systems. Noteworthy, the observed deviation from the simulated FF (~63%) of the PCE10:O-IDTBR system is caused by the field dependent charge generation, which explains the higher PCE found by the simulation, as the field dependence of charge generation is not taken into account in the simulation. In summary, our spectroscopically-determined parameters reproduce very well the experimentally-measured J-V characteristics of the solar cells, indicating that the kinetic parameters determined by transient laser spectroscopy are relevant to solar cells operating under steady-state device conditions.

Table 5: Input parameters used in drift-diffusion simulations, namely μ_h and μ_e from SCLC measurements, IQE_{avg} (IQE averaged), $\beta_{Langevin}$ calculated from mobilities, the recombination reduction-factor $\zeta = \beta_{TDCF}/\beta_{Langevin}$ used in the simulation of OPV solar cells, and J_{SC}, V_{OC}, and FF values resulting from the Setfos simulation.

System	μ_h ($cm^2V^{-1}s^{-1}$)	μ_e ($cm^2V^{-1}s^{-1}$)	IQE_{avg} (%)	$\beta_{Langevin}$ cm^3s^{-1}	ζ	J_{SC} ($mAcm^{-2}$)	V_{OC} (V)	FF	PCE (%)
O-IDTBR	2.0×10^{-4}	4.2×10^{-5}	61	1.3×10^{-10}	1.7	13.34	1.07	0.63	9.1
O-IDTBCN	9.8×10^{-4}	5.2×10^{-4}	70	8.2×10^{-10}	0.02	17.44	0.74	0.71	9.3

DFT calculations of energetic landscape

Here, we aim to understand further the solar cell characteristics, in particular the origin of V_{OC} differences, and we link those differences to the acceptors' energetic landscape, specifically their quadrupole moments, as determined by DFT calculations. The V_{OC} difference of ~0.35 V between the two BHJ systems can be readily traced to the difference in calculated EAs of the two NFAs in the gas phase, calculated to -2.74 eV for O-IDTBR and -3.09 eV for O-IDTBCN, yielding ΔEA = 0.35 eV. The calculated energy levels are shown as dashed straight lines in Figure 7. This

difference translates into a similar difference of the ionization energies (IEs) of molecules in the bulk (thin film), where O-IDTBR is stabilized by 0.72 eV and O-IDTBCN by 0.65 eV. In the film, both NFAs exhibit comparably small energetic disorder as indicated by the narrow, practically Gaussian, density of states (DOS), also shown in Figure 7.

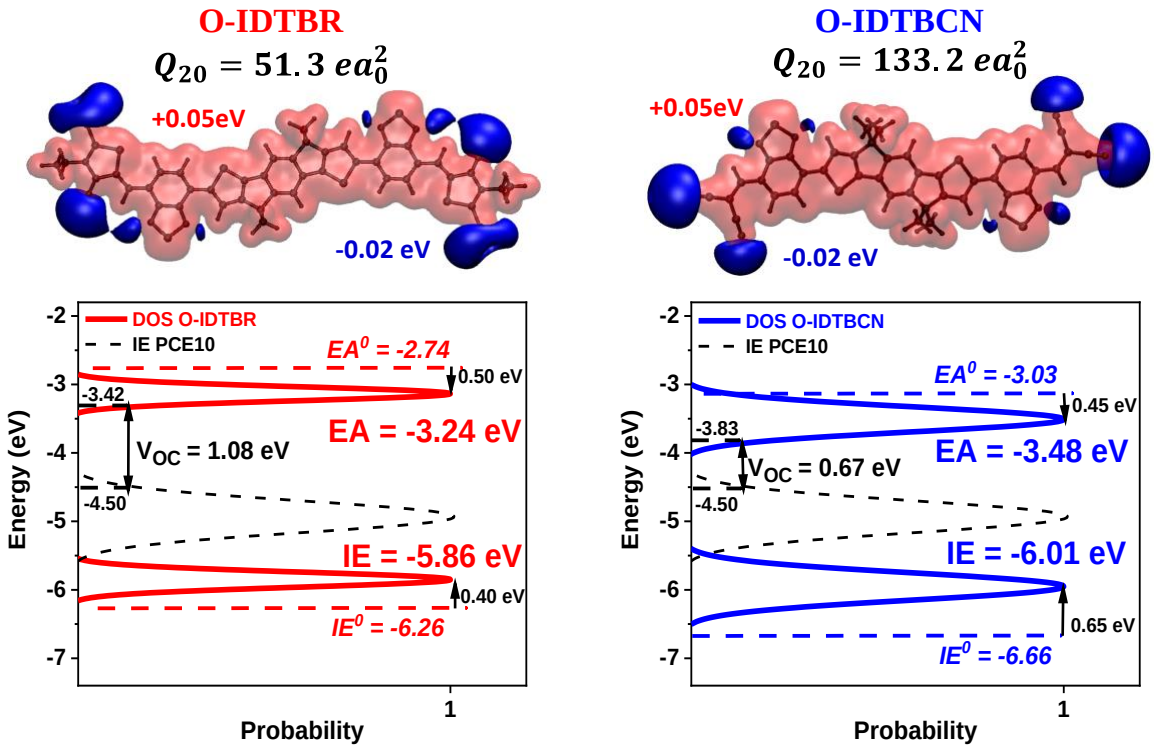

Figure 7: (Top panel) Chemical structures of O-IDTBR and O-IDTBCN with their electrical potential isosurfaces at -0.02 eV (blue) and +0.05 eV (red). Quadrupole moments (Q_{20}) are given in Debye / Angstrom, along principal axes of the quadrupole tensor. The z-axis is perpendicular to the conjugated core (blue arrow), x-axis is parallel to the long axis of molecule (red arrow). (Bottom panel) Acceptors (O-IDTBR, O-IDTBCN) EA and IE and donor (PCE10) IE, calculated density of states (DOS), and position of the Fermi level for electrons and holes, respectively (horizontal dashed lines). The V_{OC} is indicated by vertical solid arrows.

Assuming a typical concentration of charges under 1-sun illumination is ~10^{16} cm^{-3}, we obtain chemical potentials for electrons and holes of 3.62 eV and 3.96 eV for O-IDTBR and O-IDTBCN,

respectively. The difference of these chemical potentials is in line with the ca. 0.35 V difference in V_{OC} of the two blends.

Next, we focus on differences in the non-geminate charge recombination. We have previously shown that molecular quadrupoles result in energy level bending at the donor-acceptor interface. [6, 40-42] This bending creates an energy barrier for the CT state formation. The height of the barrier is proportional to the molecular quadrupole moment: here, the larger quadrupole moment of O-IDTBCN (133.2 ea_0^2) as compared to that of O-IDTBR (51.3 ea_0^2) leads to a larger energy level bending, and hence a larger energy barrier for charge recombination. In fact, we can estimate the difference of the recombination barriers from the experimentally-determined non-geminate recombination coefficients, $\beta_{\mathrm{O-IDTBCN}} = 1.7 \times 10^{-11}\,\mathrm{cm^3 s^{-1}}$ and $\beta_{\mathrm{O-IDTBR}} = 2.5 \times 10^{-10}\,\mathrm{cm^3 s^{-1}}$, as $\Delta B = k_B T \ln\left(\frac{\beta_{\mathrm{O-IDTBR}}}{\beta_{\mathrm{O-IDTBCN}}}\right) \sim$ 0.07 eV.

Finally, we turn to differences in geminate recombination. Even without considering the quantum-chemical details, such as the differences in the hole/electron transfer rates leading to the CT state recombination, we can state that the CT state dissociation is more efficient in PCE10:O-IDTBCN. As a matter of fact, the difference in the energy level bending reduces the CT state dissociation energy of PCE10:O-IDTBCN by 0.07 eV as compared to PCE10:O-IDTBR. Faster dissociation shifts the kinetic competition between dissociation and recombination towards dissociation, and hence less geminate recombination occurs in PCE10:O-IDTBCN. The difference in the dissociation barriers also explains the observation of field-dependent charge generation in the PCE10:O-IDTBR blends. In contrast, the CT state dissociation in PCE10:O-IDTBCN is more efficient when compared to that of PCE10:O-IDTBR, since the CT state binding energy is lowered by 0.07 eV. The external electric field (internal field in OPV devices) reduces this binding energy, in turn leading to more efficient free charge generation in the presence of weak electric fields. Consequently, this causes the lower FF in PCE10:O-IDTBR blends compared to PCE10 blends with O-IDTBCN as acceptor.

Conclusion

In BHJ donor:non-fullerene acceptor based blends, the IE level offset and quadrupole moments of the blends' components impact exciton quenching, charge generation, and charge recombination. We compared two systems that use the same common donor polymer, PCE10, combined with either a low quadrupole moment acceptor, O-IDTBR, or a high quadrupole moment acceptor, O-IDTBCN. Changing from a low quadrupole moment acceptor to a high quadrupole moment acceptor increased the exciton quenching efficiency, reduced monomolecular recombination losses, led to field-independent charge generation, and lowered non-geminate losses of free charges. Consequently, the IQE and thus the J_{SC} as well as the FF of devices were increased. However, large quadrupole moments are often achieved by introducing strong electron-withdrawing moieties, here dicyano-vinylene endgroups instead of rhodanine, leading to increased EAs and with that a reduced IE – EA gap, lowering the energy of interfacial CT states, and thus causing lower V_{OC} in devices. The lower CT energy increased non-radiative recombination losses to the expense of radiative CT state recombination, yet the total energy loss remained similar and in excess of 0.6 eV. Our study adds further insight into the complexity of the interplay between the local energetic landscape and the device photophysics in NFA-based systems. It demonstrates how important fine-tuning of the NFA energetics is, specifically of the acceptors' quadrupole moments, to achieve high charge generation yields, field-independent CT state dissociation, and reduced recombination, prerequisites to enhance further the device performance of NFA-based systems. However, further studies are required that account also for the donor's quadrupole moment in NFA-based systems to develop a more complete picture of the complex interplay of the materials' energetic landscape and the corresponding blends' photophysics.

Experimental Section

UV-Vis spectroscopy: The steady-state absorption measurements were conducted using a Cary 5000 UV-visible spectrometer (Agilent Technologies).

Electroluminescence (EL): Steady-state EL measurements were performed with a home-built EL spectroscopy setup inside a nitrogen-filled glovebox. The OSC devices with an active area of 0.1 cm^2 were biased with a DC voltage using a source-measure unit (Keithley 2420) similar to or lower than the V_{OC} of the cells obtained under 1 sun illumination. The EL was collected by a collimator lens and coupled into an optical fiber bundle connected to a spectrograph (Princeton Instruments SP-2300). The spectrograph was equipped with a silicon (PIX100BRX) and LN2-cooled InGaAs (PYR1024) detector array. Wavelength calibration was performed with a Ne/Ar light source (Princeton Instruments IntelliCal).

***Sensitive external quantum efficiency (sEQE)*:** The sEQE spectra of devices were collected at short-circuit conditions using monochromatic illumination from a combination of a monochromator and Xenon arc lamp. An optical chopper modulated the light beam with a frequency of 275 Hz, and the device photocurrent was measured as a function of the incident photon energy (wavelength) using a lock-in amplifier (Stanford Instruments SR 830), and the light intensity was determined using intensity-calibrated Ge and Si photodiodes.

Ultrafast time-resolved measurements: Transient absorption (TA) spectroscopy was carried out using a home-built pump-probe setup. Two distinct configurations of the setup were applied for either short delay, namely 100 fs to 8 ns experiments, or long delay, namely 1 ns to 100 μs delays, as described below.

For the 1 ns to 100 μs delay (long delay) TA measurements in the range covering 500-1500 nm, we used the fundamental 800 nm output of titanium:sapphire amplifier (Coherent LEGEND DUO, 4.5 mJ, 3 kHz, 100 fs) focused onto a sapphire crystal, thereby generating a white-light supercontinuum from 500 to 1500 nm. However, the excitation light (pump pulse) was provided by an actively Q-switched Nd:YVO_4 laser (INNOLAS picolo AOT) frequency-doubled to provide pulses at 532 nm. The laser was triggered by an electronic delay generator (Stanford Research Systems DG535), itself triggered by the TTL sync from the Legend DUO, allowing control of the delay between pump and probe with a jitter of roughly 100 ps.

Pump and probe beams were focused on the sample, which was kept under a dynamic vacuum of $<10^{-5}$ mbar. The transmitted fraction of the white light was guided to a custom-made prism spectrograph (Entwicklungsbüro Stresing) where a prism dispersed it onto a 512 pixel NMOS linear image sensor (HAMAMATSU S8381-512). The probe pulse repetition rate was 3 kHz, directly generated at 1.5 kHz frequency (1 ns to 100 μs delays), while the detector array was read out at 3 kHz. Adjacent diode readings corresponding to the transmission of the sample after excitation and in the absence of an excitation pulse were used to calculate ΔT/T. Measurements were averaged over several thousand shots to obtain a good signal-to-noise ratio. The chirp induced by the transmissive optics was corrected with a home-built Matlab code by revaluating for each wavelength the delay at which pump and probe are simultaneously arriving on the sample as the time of the signal amplitude.

Time-resolved photoluminescence spectroscopy (TR-PL): For TR-PL experiments samples were excited with the wavelength-tunable output of an OPO (Radiantis Inspire HF-100), itself pumped by the fundamental of a Ti:sapphire fs-oscillator (Spectra Physics MaiTai eHP) at 820 nm. The repetition rate of the fs pulses was adjusted by a pulse picker (APE Pulse Select). Typical pulse energies were in the range of 700 nJ. The PL of the samples was collected by an optical telescope (consisting of two plano-convex lenses) and focused on the slit of a spectrograph (PI Spectra Pro SP2300) and detected with a Streak Camera (Hamamatsu C10910) system with a temporal resolution of 1.4 ps. The data was acquired in photon counting mode using the Streak Camera software (HPDTA) and exported to Origin Pro 2020 for further analysis.

Time delayed collection field (TDCF): The home-built TDCF setup uses the second harmonic (532 nm) of an actively Q-switched sub-ns Nd:YVO_4 laser (INNOLAS picolo AOT) operating at 5 kHz as excitation. To minimize the RC response time (typically few nanoseconds), a small device area of 1 mm^2 is used. The samples were measured under dynamic vacuum conditions to avoid any degradation. A Keysight S1160A functional generator was used to provide the pre-bias and extraction bias, while a Keysight four channel digital oscilloscope was used to measure the current response of the device.

***Device Fabrication*:** Inverted bulk heterojunction solar cells were fabricated with device configuration of ITO/ZnO/Active layer/MoO_3/Ag. Performance of two different active layers of PCE10: O-IDTBR and PCE10: O-IDTBCN in BHJ solar cells were studied in this paper. Glass

substrates with pre-patterned indium tin oxide (ITO, 16 Ω sq^{-1}) were first cleaned with dilute Extran 300 detergent solution for 20 min in ultrasonic bath. Samples were rinsed in flowing deionized water for 5 min followed by sequential bath of acetone and isopropanol for 15 min each. In next step, these cleaned samples were exposed to UV-ozone plasma cleaning for 15 min. A thin layer of ZnO is spin coated (4000 rpm) using the ZnO precursor solution prepared from established procedure.[9] The films were baked at 150°C for 15 min in air to give the film thickness of 30-35 nm. The ZnO films are transferred into the glovebox for active layer deposition. The active layer solutions were prepared a day before deposition using polymer PCE10 (Purchased from 1-material) as donor mix with O-IDTBR and O-IDTBCN as acceptors. The donor and acceptors were dissolved in chlorobenzene (CB) ratio of 1:2 (by weight), with an overall concentration of 30 $mgmL^{-1}$ by 7-8 hrs stirring at temperature of 60° C. The active layers were spin coated over the ZnO coated substrates at 2000 rpm and 1500 rpm, respectively to provide the film thickness of ~ 90 nm. PCE10:O-IDTBCN films are subjected to annealing at 100°C for 10 minutes. Afterwards, the films were transferred in a thermal evaporator for the evaporation of a 8 nm MoO_3 followed by 100 nm Ag top electrode with deposition rates of 0.25 Å s^{-1} and 0.5 Å s^{-1}, respectively through a shadow mask yielding active areas of 0.1 cm^2 in each device.

***Device Characterization*:** J-V measurements of solar cells were performed in the glovebox with a Keithley 2400 source meter and an Oriel Sol3A Class AAA solar simulator calibrated to one sun, AM1.5 G, with a KG-5 silicon reference cell certified by Newport. The charge carrier (hole and electron) mobilities of PCE10:O-IDTBR and PCE10:O-IDTBCN BHJ devices were determined by fitting the dark currents of hole/electron-only diodes to the space-charge-limited current (SCLC) model. Hole-only diode configuration: Glass/ITO/PEDOT:PSS/BHJ/MoO_3/Ag. Electron-only diode configuration: Glass/ITO/ZnO/BHJ/LiF/Al. The external quantum efficiency (EQE) measurements were performed at zero bias by illuminating the device with a monochromatic light supplied from a Xenon arc lamp in combination with a dual-grating monochromator.

Space-charge-limited current (SCLC): The charge carrier (hole and electron) mobilities of PCE10:O-IDTBR and PCE10:O-IDTBCN BHJ devices were determined by fitting the dark

currents of hole/electron-only diodes to the space-charge-limited current (SCLC) model. For hole-only we used diode configuration: Glass/ITO/PEDOT:PSS/BHJ/MoO_3/Ag, and for electron-only the diode configuration: Glass/ITO/ZnO/BHJ/LiF/Al was implemented.

Ultraviolet photoelectron spectroscopy (UPS) and low energy inverse photoemission spectroscopy (LE-IPES) (near UV (NUV) range ~4.5 eV): Spectra were acquired in *ScientaOmicron* multiprobe ultrahigh vacuum (UHV) (10^{-9} mbar) system to determine the IE and EA respectively of O-IDTBCN, O-IDTBR and PCE10 films of 10 nm pristine films on Au. The substrate for film deposition was Au (100nm) Si(n-type), with the Au sputtered with an Angstrom evaporation/sputter tool. Solutions of 2-5 mg·ml^{-1} in chloroform were prepared and stirred overnight in a glove box and then spin-coated (3000-5000 rpm for 1 minute) onto an Ar+ ion sputtered Au substrate and then transferred to UHV for analysis. The organic small molecule/polymer film thickness was 10-20 nm. UPS was performed with a vacuum ultraviolet (VUV) He (1) discharge line 21.22 eV (*focus*) and a Sphera II EAC 125 7-channeltron electron analyser using a 5 eV pass energy. The sample was positioned at 0° with respect to the analyzer-to-sample plane. Fermi level calibration was performed using a clean metallic Ag foil. An in-house built UHV LE-IPES set-up was used, operating in the Bremsstrahlung Isochromatic Mode (BIS). This consisted of a BaO cathode electron source (*Staib*), with a dispersion of 0.25-0.5 eV directed at 0^o with respect to the sample plane operating at 20-30 eV. A -20V bias was applied to the sample and light collected with an internal vacuum collimating lens and external focusing lens with a 4.43 eV (280nm) (*Semrock*) band pass filter. A state PMT *Hamamatsu R585* detector was used.

***Simulations of morphologies, biases, and solid-state IEs*:** The simulation approach consists of the following subsequent steps: (i) quantum chemical calculations of isolated donor and acceptor molecules in the gas phase, (ii) force-field parameterization and molecular dynamics (MD) simulations of donor and acceptor crystals, and (iii) calculations of the solid-state electrostatic contribution to the gas phase IE.

Gas-phase quantum chemical calculations:

We performed density functional theory (DFT) calculations using the B3LYP functional and 6-311g(d,p) basis set as implemented in the GAUSSIAN package. [43] Some of the solubilizing alkyl

groups were removed to reduce the computational effort. Optimized molecule configurations were used to calculate atomic partial charges via the Merz-Kollman scheme and to parameterize polarizable force fields for the solid state IE evaluation. [44] All acceptor molecules are neutral and have zero dipole moment, while their quadruple moments are nonzero.

Force-field parameterization and molecular dynamics simulations:

Morphology simulations were performed using the GROMACS simulation package. [45] We have adapted the OPLS-AA force-field, [46-48] parameterizing missing improper and torsional potentials by scanning the cross-sections of the potential energy surfaces using DFT (at B3LYP/6-31g(d,p) level). All quantum-chemical calculations were performed using the GAUSSIAN 09 package. [43]

Since all Lennard–Jones parameters were taken from the OPLS-AA, the combination rules and fudge-factor of 0.5 were used for 1-4 interactions. The long-range electrostatic interactions were treated by using a smooth particle mesh Ewald technique. All calculations were performed in the NPT ensemble using the canonical velocity-rescaling thermostat and the Berendsen barostat, [49,50] as implemented in the GROMACS simulation package [52] Initial cell parameters and atomic positions were obtained from random start configuration. To obtain the equilibrated morphology, the simulation box of about 300 molecules (this parameter varies for different acceptors) was exposed to 400K for 30 ns with a time step of 0.001 ps.

Calculation of electrostatic contribution to the energy profile in the gas phase:

Using the molecular dynamics trajectories, the site energies were evaluated in a perturbative way, starting from the gas-phase quantum chemical calculations and then taking into account environmental effects as a perturbation. The total site energies were obtained by adding the electrostatic and induction energies to the gas phase ionization potential of a molecule, i.e., the ionization potential in the vacuum, the electrostatic interaction energy of partial charges, and the contribution due to polarization. The electrostatic and induction contributions to site energies were calculated self-consistently using the Thole model on the basis of the atomic polarizabilities and distributed multipoles obtained by using the GDMA program for a cation and a neutral molecule. [51-53] This approach, in combination with an aperiodic inclusion of charges to a neutral periodic morphology, is available in the VOTCA-CTP package. [54,55]

Bias potential due to charge-quadrupole interactions:

The interfacial bias potential (energy level bending) is the manifestation of the charge-quadrupole interactions and the interfacial concentration gradient (an electron at the interface interacts with a smaller density of acceptors dispersed in the donor phase then an electron farther away from the interface). The range and energy level bending direction depend on the mutual orientations, the π-π stacking distance, and values of the quadrupole tensor of the acceptor and donor. [40,56,57] The bias potential therefore depends of the solid-state contribution to energy levels in vacuum as well as geometrical parameters of the interface, such as its width and roughness.

More specifically, the energy level bending in the acceptor phase is proportional to the electrostatic (crystal) field created by the molecules at the interface and its vicinity. Assuming that the structure of the donor-acceptor interface is similar for all systems, and that the molecular alignment is the same at the interface and in the bulk, we can rank bias potentials by evaluating the electrostatic contribution (crystal field) in the bulk of the film. [6]

Spectroelectrochemical experiments: Spectroelectrochemistry in solution was performed using a three electrodes home-made cell. Electrochemical measurements (cyclic voltammetry and chronoamperometry) were carried out using a platinum planar disk working electrode (Ø = 3 mm), a platinum wire counter electrode and a silver wire as a quasi-reference electrode with a Biologic SP-150 potentiostat driven by the EC-Lab software including ohmic drop compensation. Experiments were recorded in dry HPLC-grade dichloromethane with tetrabutylammonium hexafluorophosphate (Bu4NPF6, electrochemical grade, Fluka) as supporting electrolyte. All solutions were prepared and transferred into the spectroelectrochemical cell in a glove box containing dry, oxygen-free (<1 ppm) argon, at room temperature (293 K). In order to have a perfect correlation between electrochemical and spectrophotometric data, measurements were carried out with thin layer conditions, i.e. with distance of 25-75 µm between the surface of the working electrode and the optical window.

Spectrophotometric measurements were carried out in direct reflection mode on the working electrode with a homemade setup composed of Princeton Instruments components (light sources, fibers, monochromators, spectroscopy camera, and software). The connection between the light source, the cell, and the spectrophotometer was ensured through a "Y-shaped" optical fiber bundle: 18 fibers guided the light to the cell, and 19 fibers collected the reflected light from the cell to the

visible (320-1080 nm / maximum acquisition frequency 2 MHz) and NIR (900-1700 nm / maximum acquisition frequency 2 MHz) detectors.

Author Contributions

J.I.K. and M.A.A. contributed equally to this work.

Supporting Information

Supporting Information is available from the Online Library or from the authors.

Acknowledgements

This publication is based upon work supported by the King Abdullah University of Science and Technology (KAUST) Office of Sponsored Research (OSR) under Award No: OSR-2018-CARF/CCF-3079 and Award No. OSR-CRG2018-3746. De. A. acknowledges funding from the BMBF grant InterPhase and MESOMERIE (FKZ 13N13661, FKZ 13N13656) and the European Union Horizon 2020 research and innovation program ‘‘Widening materials models’ under Grant Agreement No. 646259 (MOSTOPHOS). De. A. also acknowledges the KAUST PSE Division for hosting his sabbatical in the framework of the Division’s Visiting Faculty program. A.M. acknowledges funding from the European Union’s Horizon 2020 research and innovation program under the Marie Skłodowska-Curie grant agreement No 844655 (SMOLAC). J.I.K. and F.L. thank R. Lohmann and D. Gottlieb for their contributions to the development of the EL spectroscopy setup.

Notes

The authors declare no competing financial interest.

Received: ((will be filled in by the editorial staff))

Revised: ((will be filled in by the editorial staff))

Published online: ((will be filled in by the editorial staff))

AUTHOR INFORMATION

Corresponding Authors email:

frederic.laquai@kaust.edu.sa

jafar.khan@kaust.edu.sa

References

[1] Y. Cui, H. Yao, J. Zhang, T. Zhang, Y. Wang, L. Hong, K. Xian, B. Xu, S. Zhang, J. Peng, Z. Wei, F. Gao, J. Hou, *Nat. Commun.* **2019**, *10*, 2515.

[2] B. Fan, D. Zhang, M. Li, W. Zhong, Z. Zeng, L. Ying, F. Huang, Y. Cao, *Sci. China Chem.* **2019**, *62*, 746.

[3] J. Yuan, Y. Zhang, L. Zhou, G. Zhang, H.-L. Yip, T.-K. Lau, X. Lu, C. Zhu, H. Peng, P. A. Johnson, M. Leclerc, Y. Cao, J. Ulanski, Y. Li, Y. Zou, *Joule* **2019**, *3*, 1140.

[4] Y. Lin, B. Adilbekova, Y. Firdaus, E. Yengel, H. Faber, M. Sajjad, X. Zheng, E. Yarali, A. Seitkhan, O. M. Bakr, A. El-Labban, U. Schwingenschlögl, V. Tung, I. McCulloch, F. Laquai, T. D. Anthopoulos, *Adv. Mater.* **2019**, *31*, 1902965.

[5] Q. Liu, Y. Jiang, K. Jin, J. Qin, J. Xu, W. Li, J. Xiong, J. Liu, Z. Xiao, K. Sun, S. Yang, X. Zhang, L. Ding, *Sci. Bull.* **2020**, *65*, 272.

[6] S. Karuthedath, J. Gorenflot, Y. Firdaus, N. Chaturvedi, C. S. P. De Castro, G. T. Harrison, J. I. Khan, A. Markina, A. H. Balawi, T. A. D. Peña, W. Liu, R.-Z. Liang, A. Sharma, S. H. K. Paleti, W. Zhang, Y. Lin, E. Alarousu, D. H. Anjum, P. M. Beaujuge, S. De Wolf, I. McCulloch, T. D. Anthopoulos, D. Baran, D. Andrienko, F. Laquai, *Nat. Mater.* **2020**, *20*, 378

[7] M. Chen, D. Liu, W. Li, R. S. Gurney, D. Li, J. Cai, E. L. K. Spooner, R. C. Kilbride, J. D. McGettrick, T. M. Watson, Z. Li, R. A. L. Jones, D. G. Lidzey, T. Wang, *ACS Appl. Mater. Interfaces* **2019**, *11*, 26194.

[8] A. Wadsworth, H. Bristow, Z. Hamid, M. Babics, N. Gasparini, C. W. Boyle, W. Zhang, Y. Dong, K. J. Thorley, M. Neophytou, R. S. Ashraf, J. R. Durrant, D. Baran, I. McCulloch, *Adv. Funct. Mater.* **2019**, *29*, 1808429

[9] X. Du, T. Heumueller, W. Gruber, A. Classen, T. Unruh, N. Li, C. J. Brabec, *Joule* **2019**, 3, 215.

[10] X. Wang, A. Tang, J. Yang, M. Du, J. Li, G. Li, Q. Guo, E. Zhou, *Sci. China Chem.* **2020**, *63*, 1666.

[11] A. Tang, B. Xiao, Y. Wang, F. Gao, K. Tajima, H. Bin, Z.-G. Zhang, Y. Li, Z. Wei, E. Zhou, *Adv. Funct. Mater*. **2018**, *28*, 1704507.

[12] H. Yao, Y. Cui, R. Yu, B. Gao, H. Zhang, J. Hou, *Angew.Chem. Int. Ed.* **2017**, *56*, 3045;

[13] X. Che, Y. Li, Y. Qu, S. R. Forrest, *Nat. Energy* **2018**, *3*, 422.

[14] W. Zhao, S. Li, H. Yao, S. Zhang, Y. Zhang, B. Yang, J. Hou, *J. Am. Chem.l Soc.* **2017**, *139*, 7148.

[15] S. Holliday, R. S. Ashraf, A. Wadsworth, D. Baran, S. A. Yousaf, C. B. Nielsen, C.-H. Tan, S. D. Dimitrov, Z. Shang, N. Gasparini, M. Alamoudi, F. Laquai, C. J. Brabec, A. Salleo, J. R. Durrant, I. McCulloch, *Nat. Commun.* **2016**, *7*, 11585.

[16] M. A. Alamoudi, J. I. Khan, Y. Firdaus, K. Wang, D. Andrienko, P. M. Beaujuge, F. Laquai, *ACS Energy Lett.* **2018**, *3*, 802.

[17] A. H. Balawi, Z. Kan, J. Gorenflot, P. Guarracino, N. Chaturvedi, A. Privitera, S. Liu, Y. Gao, L. Franco, P. Beaujuge, F. Laquai, *Sol. RRL* **2020**, *4*, 2000181.

[18] S. Karuthedath, J. Gorenflot, A. Melianas, Z. Kan, M. Kemerink, F. Laquai, *J. Phys. Chem. Lett.* **2020**, *11*, 2838.

[19] S. M. Menke, N. A. Ran, G. C. Bazan, R. H. Friend, *Joule* **2018**, *2*, 25.

[20] Y. Yang, W. Chen, L. Dou, W.-H. Chang, H.-S. Duan, B. Bob, G. Li, Y. Yang, *Nat. Photonics* **2015**, *9*, 190.

[21] J. I. Khan, R. S. Ashraf, M. A. Alamoudi, M. N. Nabi, H. N. Mohammed, A. Wadsworth, Y. Firdaus, W. Zhang, T. D. Anthopoulos, I. McCulloch, F. Laquai, *Sol. RRL* **2019**, *3*, 1900023.

[22] I. A. Howard, R. Mauer, M. Meister, F. Laquai, *J. Am. Che. Soc.* **2010**, *132*, 14866.

[23] J. Jaumot, R. Gargallo, A. de Juan, R. Tauler, *Chemom. Intell. Lab. Syst.* **2005**, *76*, 101.

[24] D. W. Gehrig, I. A. Howard, F. Laquai, *J. Phys. Chem. C* **2015**, *119*, 13509.
[25] F. Etzold, I. A. Howard, N. Forler, A. Melnyk, D. Andrienko, M. R. Hansen, F. Laquai, *Energy Environ. Sci.* **2015**, *8*, 1511.
[26] M. Azzouzi, T. Kirchartz, J. Nelson, *Trends Chem.* **2019**, *1*, 49.
[27] K. Tvingstedt, K. Vandewal, A. Gadisa, F. Zhang, J. Manca, O. Inganäs, *J. Am. Chem. Soc.* **2009**, *131*, 11819;
[28] D. Veldman, S. C. J. Meskers, R. A. J. Janssen, *Adv. Funct. Mater.* **2009**, *19*, 1939.
[29] M. A. Faist, T. Kirchartz, W. Gong, R. S. Ashraf, I. McCulloch, J. C. de Mello, N. J. Ekins-Daukes, D. D. C. Bradley, J. Nelson, *J. Am. Chem. Soc.* **2012**, *134*, 685.
[30] J. Mooney, P. Kambhampati, *J. Phys. Chem. Lett.* **2013**, *4*, 3316.
[31] K. Vandewal, K. Tvingstedt, A. Gadisa, O. Inganäs, J. V. Manca, *Phys. Rev. B* **2010**, 81, 125204.
[32] M. Babics, T. Duan, A. H. Balawi, R.-Z. Liang, F. Cruciani, I.-D. Carja, D. Gottlieb, I. McCulloch, K. Vandewal, F. Laquai, P. M. Beaujuge, *ACS Appl. Energy Mater.* **2019**, *2*, 2717.
[33] U. Rau, *Phys. Rev. B*, **2007**, *76*, 085303.
[34] M. Azzouzi, J. Yan, T. Kirchartz, K. Liu, J. Wang, H. Wu, J. Nelson, *Phys. Rev. X* **2018**, 8, 031055.
[35] J. Benduhn, K. Tvingstedt, F. Piersimoni, S. Ullbrich, Y. Fan, M. Tropiano, K. A. McGarry, O. Zeika, M. K. Riede, C. J. Douglas, S. Barlow, S. R. Marder, D. Neher, D. Spoltore, K. Vandewal, *Nat. Energ.* **2017**, *2*, 17053.
[36] R. Mauer, I. A. Howard, F. Laquai, *J. Phys. Chem. Lett.* **2011**, *2*, 1736.
[37] J. Kniepert, I. Lange, N. J. van der Kaap, L. J. A. Koster, D. Neher, *Adv. Energy Mater.* **2014**, *4*, 1301401.
[38] S. Albrecht, W. Schindler, J. Kurpiers, J. Kniepert, J. C. Blakesley, I. Dumsch, S. Allard, K. Fostiropoulos, U. Scherf, D. Neher, *Phys. Chem. Lett.* **2012**, *3*, 640.
[39] J. I. Khan, Y. Firdaus, F. Cruciani, S. Liu, T. D. Anthopoulos, P. M. Beaujuge, F. Laquai, *J. Phys. Chem. C* **2020**, *124*, 10420
[40] C. Poelking, D. Andrienko, *J. Am. Chem. Soc.* **2015**, *137*, 6320.
[41] C. Poelking, M. Tietze, C. Elschner, S. Olthof, D. Hertel, B. Baumeier, F. Würthner, K. Meerholz, K. Leo, D. Andrienko, *Nat. Mater.* **2014**, *14*, 434.
[42] L. Perdigón-Toro, H. Zhang, A. Markina, J. Yuan, S. M. Hosseini, C. M. Wolff, G. Zuo, M. Stolterfoht, Y. Zou, F. Gao, D. Andrienko, S. Shoaee, D. Neher, *Adv. Mater.* **2020**, *32*, 1906763.
[43] M. J. Frisch, G. W. Trucks, H. B. Schlegel, G. E. Scuseria, M. A. Robb, J. R. Cheeseman, G. Scalmani, V. Barone, G. A. Petersson, H. Nakatsuji, X. Li, M. Caricato, A. V. Marenich, J. Bloino, B. G. Janesko, R. Gomperts, B. Mennucci, H. P. Hratchian, J. V. Ortiz, A. F. Izmaylov, J. L. Sonnenberg, Williams, F. Ding, F. Lipparini, F. Egidi, J. Goings, B. Peng, A. Petrone, T. Henderson, D. Ranasinghe, V. G. Zakrzewski, J. Gao, N. Rega, G. Zheng, W. Liang, M. Hada, M. Ehara, K. Toyota, R. Fukuda, J. Hasegawa, M. Ishida, T. Nakajima, Y. Honda, O. Kitao, H. Nakai, T. Vreven, K. Throssell, J. A. Montgomery Jr., J. E. Peralta, F. Ogliaro, M. J. Bearpark, J. J. Heyd, E. N. Brothers, K. N. Kudin, V. N. Staroverov, T. A. Keith, R. Kobayashi, J. Normand, K. Raghavachari, A. P. Rendell, J. C. Burant, S. S. Iyengar, J. Tomasi, M. Cossi, J. M. Millam, M. Klene, C. Adamo, R. Cammi, J. W. Ochterski, R. L. Martin, K. Morokuma, O. Farkas, J. B. Foresman, D. J. Fox, Wallingford, CT 2016.
[44] U. C. Singh, P. A. Kollman, *J. Computational Chem.* ***1*984**, *5*, 129.
[45] M. J. Abraham, T. Murtola, R. Schulz, S. Páll, J. C. Smith, B. Hess, E. Lindahl, *SoftwareX* **2015**, *1-2*, 19.
[46] W. L. Jorgensen, D. S. Maxwell, J. Tirado-Rives, *J. Am. Chem. Soc.* **1996**, *118*, 11225.
[47] W. L. Jorgensen, J. Tirado-Rives, *Proc. Nat. Acad. Sci. U. S. A.* **2005**, *102*, 6665.
[48] W. L. Jorgensen, J. Tirado-Rives, *J. Am. Chem. Soc.* **1988**, *110*, 1657.
[49] G. Bussi, D. Donadio, M. Parrinello, *J. Chem. Phys.* **2007**, 126, 014101.

[50] H. J. C. Berendsen, J. P. M. Postma, W. F. v. Gunsteren, A. DiNola, J. R. Haak, *J. Chem. Phys.* **1984**, *81*, 3684.
[51] B. T. Thole, *Chem. Phys.* **1981**, *59*, 341.
[52] P. T. van Duijnen, M. Swart, *Phys. Chem. A* **1998**, *102*, 2399.
[53] A. J. Stone, *J. Chem. Theory Comput*. **2005**, *1*, 1128.
[54] M. Schwarze, W. Tress, B. Beyer, F. Gao, R. Scholz, C. Poelking, K. Ortstein, A. A. Günther, D. Kasemann, D. Andrienko, K. Leo, *Science* **2016**, *352*, 1446.
[55] V. Rühle, A. Lukyanov, F. May, M. Schrader, T. Vehoff, J. Kirkpatrick, B. Baumeier, D. Andrienko, *J. Chem. Theory Comput*. **2011**, *7*, 3335.
[56] G. D'Avino, L. Muccioli, F. Castet, C. Poelking, D. Andrienko, Z. G. Soos, J. Cornil, D. Beljonne, *J. Phys. Condens. Matter* **2016**, *28*, 433002.
[57] M. Schwarze, K. S. Schellhammer, K. Ortstein, J. Benduhn, C. Gaul, A. Hinderhofer, L. Perdigón Toro, R. Scholz, J. Kublitski, S. Roland, M. Lau, C. Poelking, D. Andrienko, G. Cuniberti, F. Schreiber, D. Neher, K. Vandewal, F. Ortmann, K. Leo, *Nat. Commun.* **2019**, *10*, 2466.

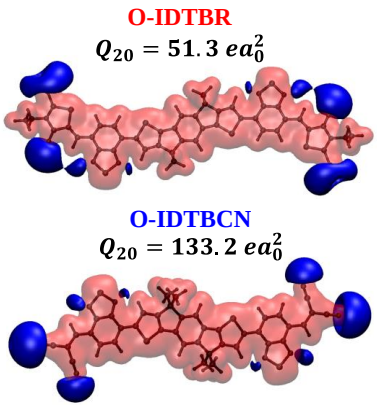

The quadrupole moment of non-fullerene acceptors (NFAs) is an important parameter, which controls exciton quenching, charge generation, and recombination in NFA-based blends. Using two structurally similar NFAs, namely O-IDTBR and O-IDTBCN, with largely different quadrupole moments (Q_{20}), the precise impact on efficiency-limiting processes is revealed by a combination of computational and transient optical and electro-optical spectroscopy studies.